

Strain and carrier transport along dislocations

Manfred Reiche^{*,1}, Martin Kittler^{2,3}, Eckhard Pippel¹, Winfried Erfurth¹, Angelika Haehnel¹, and Hartmut Uebensee⁴

¹ Max Planck Institute of Microstructure Physics, Weinberg 2, 06120 Halle, Germany

² IHP Microelectronics, Im Technologiepark 25, 15236 Frankfurt (Oder), Germany

³ Brandenburg University of Technology, JointLab IHP/BTU, Platz der Deutschen Einheit 1, 03046 Cottbus, Germany

⁴ CIS Research Institute of Microsensorics and Photovoltaics, Konrad-Zuse Straße 14, 99099 Erfurt, Germany

Received 30 September 2014, revised 1 June 2015, accepted 6 July 2015

Published online 27 July 2015

Keywords dislocation, strain, carrier transport

* Corresponding author: e-mail reiche@mpi-halle.de, Phone: +49 345 5582 676, Fax: +49 30 5582 578, Web: www.mpi-halle.de

A significant increase of the drain current is verified if defined numbers and types of dislocations are present in the channel of MOSFETs. For pMOSFETs, analysed here, an enhancement by a factor of eight exists if mixed dislocations are placed in the channel. The drain current increase is caused by higher concentration and higher mobility of holes on dislocations. It is shown that cores of mixed dislocations possess uniaxial compressive strain components in the order of $\varepsilon \cong -0.1$ which are signifi-

cantly higher than in the strain field surrounding a dislocation. The exceptional high uniaxial strain results in dramatic alterations of the silicon band structure. Upward shifts of the upper valence bands appear forming a quantum wire. The generation of the quantum wire forces hole confinement along dislocations and generates a one-dimensional hole gas (1DHG). Confinement and energy quantization are assumed to be most important for the increased carrier transport along dislocations.

© 2015 WILEY-VCH Verlag GmbH & Co. KGaA, Weinheim

1 Introduction

Dislocations are one-dimensional crystal defects influencing many of the physical and mechanical properties of crystalline solids. The analysis of their electronic properties is of particular interest for semiconductor devices because randomly distributed dislocations detrimentally impact device parameters [1, 2]. Dislocations, however, exhibit also beneficial effects on device performance. For instance, defect engineering has nowadays a widespread and sophisticated application in the fabrication of microelectronic devices and other areas [3, 4]. Furthermore, well-defined arrays of dislocations in the channel of metal-oxide-semiconductor field-effect transistors (MOSFETs) result in a significant increase of the drain current (I_D) [5, 6]. The largest increase of I_D is obtained for a single dislocation [7]. In p-type silicon dislocations form channels for electrons with supermetallic conductivity which is about eight orders of magnitude higher than of the surrounding Si matrix [7].

Different models of the electronic structure of dislocations have been proposed in the past [8–10]. Experimental

investigations as well as computer simulations revealed the existence of deep and shallow levels in the gap caused by dislocations. Shallow levels are assumed to be related either to extended states (stacking faults between two partial dislocations) or states of electrons and holes trapped in the elastic deformation field around a dislocation. The response of the band structure to homogeneous elastic stresses is described by the deformation potential [11–13]. On the other hand, deep levels are assumed to be related to reconstruction defects (antiphase defects, solitons) on the dislocation core [14]. The energy of these intrinsic levels depends strongly on the geometry of the defects. Recently published results of computer simulations of the carrier transport along dislocations as well as low-temperature measurements demonstrated, however, that carriers are not located on core defects [15]. Instead, a one-dimensional electron gas exists along a dislocation [16]. This means that not the geometry of core defects is crucial for deep level generation, but the strain in the core. Strain levels of about 10%, or more, were predicted inside dislocation cores which are significantly higher than in the strain field

surrounding a dislocation [17–19]. Here, we present experimental findings and results of computer simulations of the band structure showing impressively that the high strain level in the core significantly impacts the electronic structure of a dislocation and that dislocations are well described as quantum wires.

2 Experimental

The technique to realize defined two-dimensional arrays of dislocations in thin layers (semiconductor wafer direct bonding) was described elsewhere [5, 7]. Measurements being made throughout the entire process (total reflection X-ray fluorescence, TXRF) proved impurity concentration close or below the detection limit of the method ($< 10^9$ at./cm² [20]). Impurities have been also not detected on individual dislocations by applying analytical electron microscopy (electron energy loss spectroscopy (EELS), energy-dispersive X-ray analysis, EDX).

Silicon-on-insulator (SOI) wafers (diameter 150 mm, $<100>$ orientation, buried oxide (BOX) thickness 60 nm, device layer thickness 30 nm) were used. Bonding two of them (hydrophobic conditions were applied) and subsequent annealing result in a new SOI wafer having a device layer thickness of 60 nm containing a two-dimensional dislocation network in the middle.

MOSFETs were prepared on such SOI substrates using standard CMOS processes [5, 7]. The gate length L was fixed to 1 μm , while different gate widths W were applied in order to study the effect of different dislocation numbers under the same conditions.

The defect structure was analysed by applying a probe C_s corrected scanning transmission electron microscope (STEM, FEI Titan 80-300). Local strain fields were quantified by peak-pairs analysis (PPA) of high-resolution electron microscope images.

Commercially available 2D- and 3D-device simulation packages (ATHENA/ATLAS, Silvaco) were utilized to compute MOSFET device parameters. Simulations of the band structure were performed by applying the nextnano³ simulation package [21]. The bulk band structure was calculated using 6- and 8-band- $\mathbf{k}\cdot\mathbf{p}$ -models and an empirical $\text{sp}^3\text{d}^5\text{s}^*$ tight binding model [22] taking into account strain and deformation potentials. Both, tight binding and $\mathbf{k}\cdot\mathbf{p}$ methods are frequently applied to calculate band structures in strained systems [23, 24].

3 Results and discussion

The effect of defined numbers of dislocations in the channel of nMOSFETs was studied in a previous paper [5]. An increase of the source drain current (I_{SD}) by more than a factor of 50 compared to reference devices without dislocations was proved. The increase of I_{SD} for nMOSFETs is attributed to the fact that dislocations form highly conductive channels for electrons. An increase of I_{SD} is also obtained for pMOSFETs, where, in contrast to nMOSFETs, a p-type channel exists in n-type silicon and holes are the dominant carriers. Figure 1a shows a dislocation network prepared by bonding of SOI wafers having n-type device layers. Because tilt and twist angles are almost equal (about 0.1°), reactions between the screw dislocation network and 60° dislocations exist. The transfer characteristic of a pMOSFET having such a dislocation array in the channel is shown in Fig. 1b in comparison to a reference device without dislocations (Fig. 1c). The drain current is about 16 μA at $V_{\text{GS}} = V_{\text{DS}} = -1$ V for the device with dislocations in the channel, while $I_{\text{SD}} \approx 2$ μA for the reference sample. This corresponds to an increase of I_{SD} by a factor of eight if dislocations are present in the channel of pMOSFETs. Simulations of the transfer characteristic of devices without dislocations are in good agreement with measured data if standard models for MOSFETs are applied (Fig. 1c). Modifications, however, are required to simulate the transfer characteristic of pMOSFETs with dislocations. Analogous to nMOSFETs

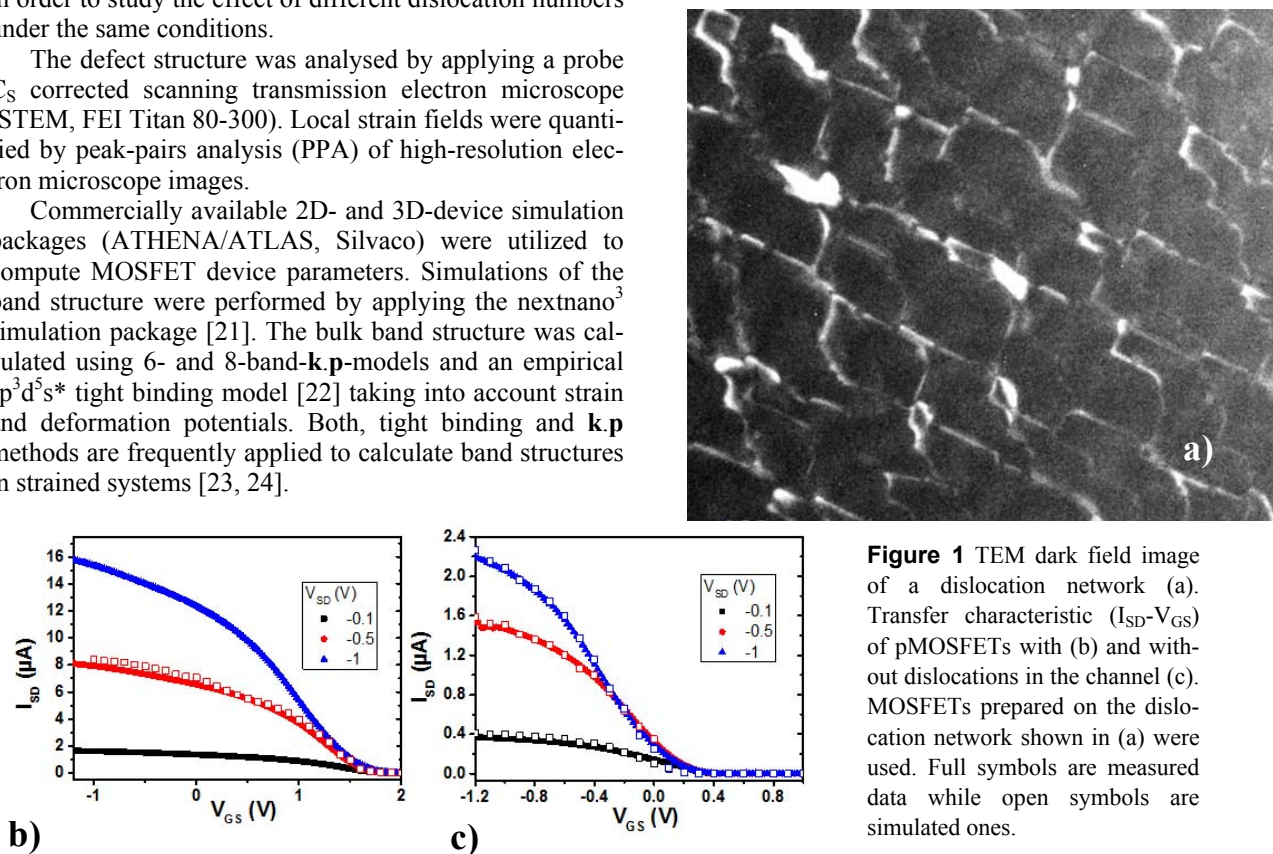


Figure 1 TEM dark field image of a dislocation network (a). Transfer characteristic ($I_{\text{SD}}-V_{\text{GS}}$) of pMOSFETs with (b) and without dislocations in the channel (c). MOSFETs prepared on the dislocation network shown in (a) were used. Full symbols are measured data while open symbols are simulated ones.

[15], dislocations are assumed as an about 2 nm thick layer (p-type doped) in the centre of the channel. Furthermore, standard mobility models describing only field-, concentration-, and temperature dependence of carriers in the inversion layer (Lombardi CVT model [25]) failed and are replaced by models which additionally consider different carrier scattering mechanisms. Here, Klaassen's unified mobility model [26, 27] was applied which includes the effects of lattice scattering, carrier-carrier scattering, and impurity scattering (with screening from charged carriers) in the dislocation layer. Using these modifications, the transfer characteristic of pMOSFETs with dislocations in the channel was successfully simulated (Fig. 1b). This refers to a strong effect of scattering mechanisms on the carrier (hole) transport along dislocations, but it is difficult to distinguish between specific scattering mechanisms in device simulations.

Further information about the carrier transport are obtained by analysis of the dislocation network. Electron microscopy of plane-view samples revealed the interaction of screw and 60° dislocations as well as their dissociation (Fig. 1). This was confirmed by detailed analysis on {110}-cross-section samples using high-resolution electron microscopy methods (high-angle annular dark field (HAADF) microscopy). Figure 2a shows a cross-section image of a typical dislocation of the network. It was shown that the dislocation is formed by the reaction of a screw and 60° dislocation lying in two different {111}-planes. Before reaction, both dislocations dissociate according to the reactions

$$\frac{a}{2} \begin{bmatrix} 101 \end{bmatrix} \rightarrow \frac{a}{6} \begin{bmatrix} 112 \end{bmatrix} + \frac{a}{6} \begin{bmatrix} 211 \end{bmatrix} \quad (1)$$

and

$$\frac{a}{6} \begin{bmatrix} 011 \end{bmatrix} \rightarrow \frac{a}{6} \begin{bmatrix} 112 \end{bmatrix} + \frac{a}{6} \begin{bmatrix} 121 \end{bmatrix}, \quad (2)$$

where Eq. (1) characterizes the dissociation of a 60° dislocation into a 30° partial (first reaction product) and a 90° partial dislocation (second product) [28]. Equation (2) denotes the dissociation of a screw dislocation into two 30° partial dislocations. The reaction of the dissociated dislocations may be described by [29]

$$\begin{aligned} & \frac{a}{6} \begin{bmatrix} 112 \end{bmatrix} + \frac{a}{6} \begin{bmatrix} 211 \end{bmatrix} + \frac{a}{6} \begin{bmatrix} 112 \end{bmatrix} + \frac{a}{6} \begin{bmatrix} 121 \end{bmatrix} \rightarrow \\ & \frac{a}{6} \begin{bmatrix} 112 \end{bmatrix} + \frac{a}{6} \begin{bmatrix} 112 \end{bmatrix} + \frac{a}{6} \begin{bmatrix} 110 \end{bmatrix}. \end{aligned} \quad (3)$$

A stick-and-ball model of the resulting defect is shown in Fig. 2b where both 30° partials (light blue colour) limit the stacking fault (dark blue) resulting from the dissociated screw dislocation. Note that only the central 30° partial dislocation is shown in Fig. 2b. The extra half plane in-

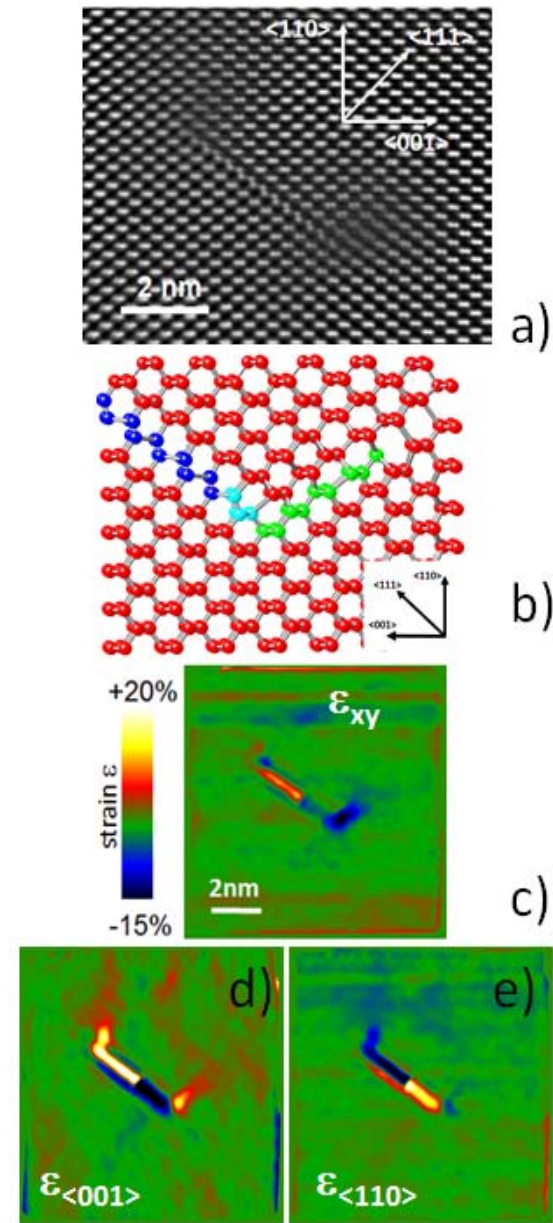


Figure 2 HAADF image of a mixed dislocation resulting from the interaction of a screw and 60° dislocation (a). A {110} cross-section sample was used for imaging. Stick-and-ball model of the defect in a projection parallel to {110} (b). The stacking fault formed by the dissociation of the screw dislocation is marked dark blue while the extra half plane induced by the 60° dislocation is plotted in green. The central partial dislocation is marked in light blue. Atoms of the undisturbed Si matrix are shown in red colour. (c) Resulting in-plane strain (ϵ_{xy}) in {110} at the dislocation shown in (a). High tensile strain of about +10% exists on the dissociated screw dislocation (red color) while the dissociated 60° dislocation shows compressive strain of about -10% (dark blue). Strain components in main directions ($\epsilon_{[001]}$ and $\epsilon_{[110]}$) are shown in (d) and (e).

duced by the 60° dislocation is marked in green. An analogous model has been also proposed by other authors [28].

As in the case of screw dislocations [7], the strain fields at individual defects are quantified by peak-pairs analysis (PPA) of high-resolution electron microscope images. This method extracts the strain ε in the defects and the surrounding area by measurement of the lattice distortion. Analyses of ε in different directions clearly proved that most of the strain is concentrated on dislocation cores (Fig. 2c). Note that strain fields around a dislocation are about two orders of magnitude lower (e.g. [30]). Uniaxial tensile strain of about 10 % exists in one part of the defect (corresponding to the original screw dislocation, red in Fig. 2c), while uniaxial compressive strain dominates the other part (dark blue colour in Fig. 2c). The uniaxial compressive strain, which is also in the order of 10 % or more, is caused by the extra half plane of the original 60° dislocation. Tight binding simulations in combination with 8-band **k.p** models proved significant alterations of the band structure with increasing uniaxial tensile strain [16]. Here, the decrease of the direct bandgap ($E_g^{(dir)}$) at the Γ -point is most important, which is mainly caused by the downward shift of the minimum of the lowest conduction band with increasing tensile strain (Fig. 3). At $\varepsilon = +0.1$, $E_g^{(dir)}$ is nearly equal the band gap of the indirect transition ($E_g^{(ind)}$) between the valence band maximum at the Γ -point and the maximum of the lowest conduction band at the Δ -point. The bandgap of $E_g^{(ind)}$ is more or less unchanged with increasing tensile strain but another indirect transition between the lowest conduction band at the L-point and the valence band maximum at the Γ -point is formed.

On the other hand, uniaxial compressive strain of a dislocation results also in substantial changes of the band

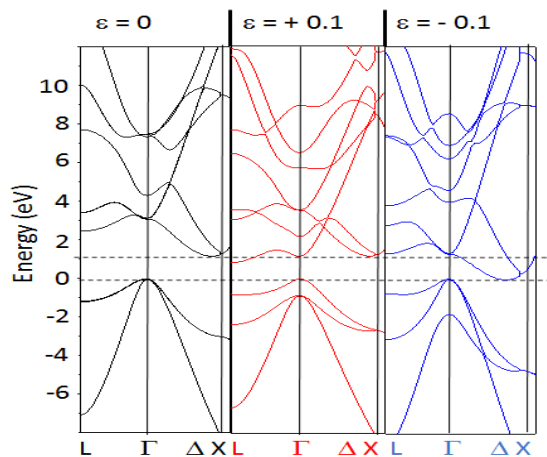


Figure 3 Schema of the band structure of unstrained ($\varepsilon = 0$) silicon (left). High tensile strain ($\varepsilon = +0.1$, middle, red) causes downward shifts of the lowest conduction band at Γ - and L-points. High compressive strain ($\varepsilon = -0.1$, right, blue) initiates shifts of the lowest conduction bands at Γ -, L-, and Δ -points. For calculation, uniaxial strain is assumed. The valence band maximum was set to zero for clarity.

structure (Fig. 3). Increasing uniaxial compressive strain yields, however, that the indirect transition between the minimum of the lowest conduction band at the Δ -point and the valence band maximum at the Γ -point decreases continuously (Fig. 4). The gap is only about 40 meV if an uniaxial compressive strain of 10% ($\varepsilon = -0.1$) is applied. The minima of the lowest conduction band at Γ and L are also shifted down with increasing compressive strain. But the band gap at the Γ -point ($E_g^{(dir)}$) is about 1.2 eV for $\varepsilon = -0.1$. An equivalent value is measured for the second indirect transition between L- and Γ -points.

Besides the shift of the conduction band reducing dramatically the gap, splitting and warping of the valence band appear if uniaxial compressive strain is applied. Both, strain-induced band splitting and warping are assumed to be main reasons of the hole mobility enhancement [31]. The in-plane dispersion of heavy holes (HH) and light holes (LH) in compressively strained silicon is shown in Fig. 5 in comparison to unstrained silicon. According to literature data [32] effective hole masses in [110]-direction of $m_{HH} = 0.55m_0$, $m_{LH} = 0.15m_0$, and $m_{SH} = 0.23m_0$ are used for unstrained Si. Applying uniaxial compressive strain, characteristic modifications of the energy dispersion of the hole bands exist (Fig. 5c, d). Especially the modification of the dispersion of the HH band is remarkable. The heavy mass contribution from the wings along $\langle 110 \rangle$ (Fig. 5a, e) is reduced if an uniaxial compressive strain along [110] is applied (Fig. 5c, f). The effective masses decrease along the strain direction and are calculated to be $m_{HH} = 0.27m_0$ and $m_{LH} = 0.12m_0$ for $\varepsilon_{[110]} = -0.1$. Note that in the presence of uniaxial strain a strong coupling of the wave functions exists and there are no longer pure HH- and LH bands [33]. The decreasing hole masses, however, are not the only reason for mobility enhancement. Among other effects, strain-induced scattering reduction is an important factor to enhance hole mobility (for instance [34, 35]). Furthermore, confinement effects are important for mobility enhancement [23]. As shown before, band structure calculations revealed local shifts of the valence and conduction bands if uniaxial

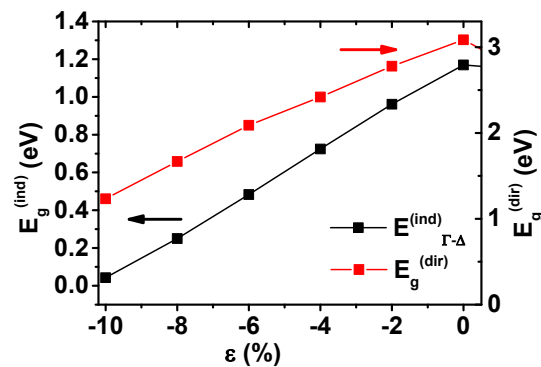


Figure 4 Direct and indirect band gaps as a function of uniaxial compressive strain along $\langle 110 \rangle$. Data extracted from tight binding simulations.

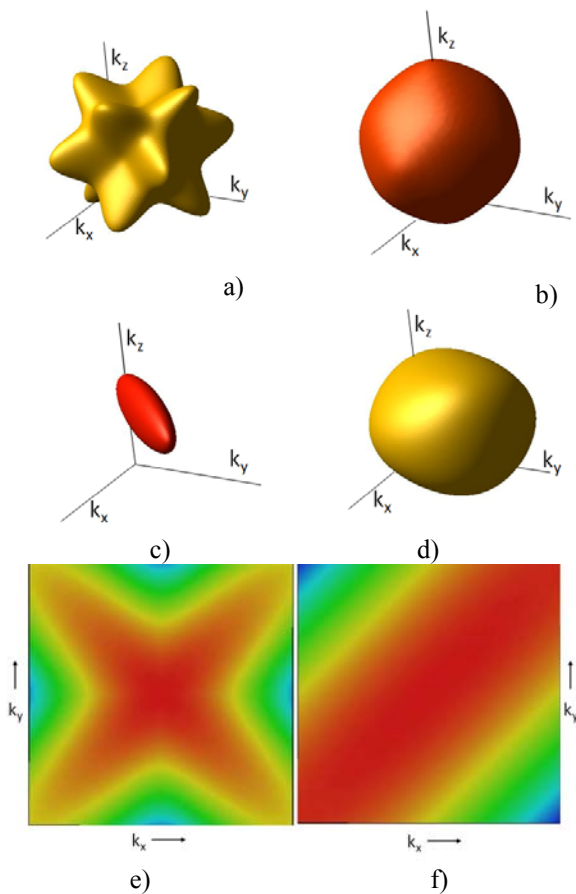


Figure 5 Energy surfaces of heavy (a, c) and light hole bands (b, d) of unstrained (a, b) and compressively strained Si (c, d). The energy dispersion of heavy holes for unstrained (e) and compressively strained Si (f) at $k_z = 0$. Uniaxial strain ($\epsilon_{\langle 110 \rangle} = -0.1$).

compressive strain is applied. The conduction band minimum at Δ shifts downward while the maxima of the upper valence bands (HH, LH) at the Γ -point shift upwards. This, on the one hand, reduces the band gap and, on the other hand, yields in a quantum wire caused by the upward shift of the valence band maxima E_{HH}^{val} and E_{LH}^{val} . A cross section through the quantum wire is schematically shown in Fig. 6 if an uniaxial compressive strain of $\epsilon_{[110]} = -0.1$ is assumed. The depth of the well formed by E_{HH}^{val} is about 330 meV while the strain-induced splitting of the heavy hole and light hole band is $E_{HH}^{val} - E_{LH}^{val} \approx 50$ meV. Solving the Schrödinger equation for an infinite cylindrical potential to model 1-dimensional wires, one obtains solutions for quantized energy levels [16, 36],

$$E_i = \frac{\hbar^2}{2m_{HH,LH}} \frac{J_0(r)^2}{R^2} \quad (i = 1, 2, \dots), \quad (4)$$

with $J_0(r)$ as the first root of the Bessel function, $m_{HH,LH}$ as the effective HH and LH masses, respectively, \hbar the

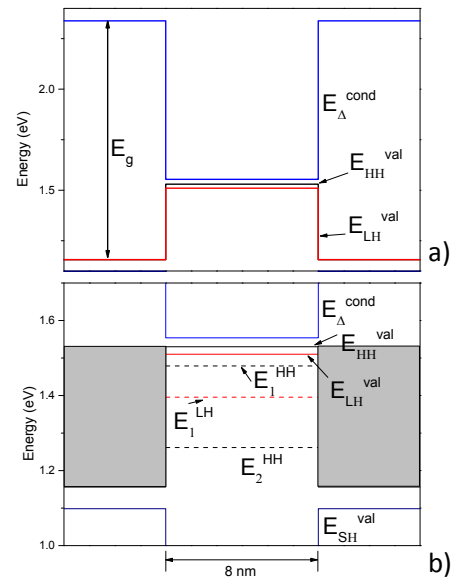


Figure 6 Band alignment for a dislocation in a pMOSFET channel. The radius of the dislocation was assumed as $R = 4$ nm. An overview about the energies at the conduction band minimum at $\Delta(E_{\Delta}^{cond})$ as well as the maxima of the upper (E_{HH}^{val}) and lower valence band (E_{LH}^{val}) extracted from band structure calculations (a). E_g is the band gap in the unstrained silicon. Detail of the valence band forming the quantum wire (b). Dashed lines characterize the first energy levels calculated for the quantum wire.

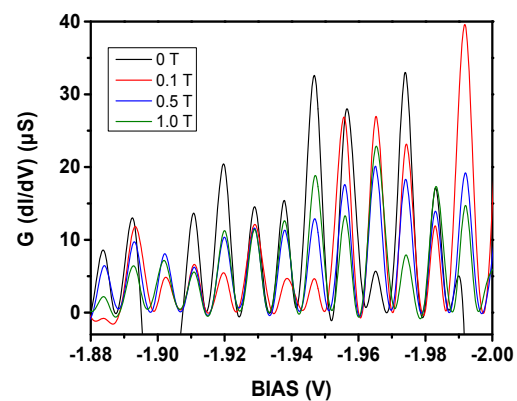


Figure 7 Evolution of Coulomb blockade oscillations with a transversal magnetic field. The strength of the magnetic field is indicated in the figure. Measurement at $T = 4$ K.

reduced Planck constant, and R as the radius of the quantum wire. With $R = 4$ nm and the calculated effective hole masses, energy levels $E_1^{HH} = 50.9$ meV and $E_2^{HH} = 268$ meV result for $m_{HH} = 0.27m_0$. For $m_{LH} = 0.12m_0$ the first energy level is $E_1^{LH} = 114$ meV (Fig. 6).

The interpretation of dislocations as quantum wires explains most of the experimental results. For screw dislocations characterized by large tensile strain, the presence of a one-dimensional electron gas was demonstrated. Their energy quantization is related to the presence of Coulomb blockades [16]. In analogy, Coulomb blockades were also obtained for mixed dislocations having a large component of uniaxial compressive strain (Fig. 7). Their existence indicates the presence of a one-dimensional hole gas (1DEG) for dislocations with uniaxial compressive strain components (edge or mixed dislocations). Here, the amplitude of Coulomb blockades is affected by a transversal external magnetic field. This is in contrast to screw dislocations where variations of the Coulomb blockade oscillations appear only if longitudinal magnetic fields are applied. An explanation is the difference in the direction of Burgers vector and dislocation line. While for screw dislocations the Burgers vector is parallel to the dislocation line direction (and therefore the tensile strain field is parallel to the dislocation line), different directions exist for Burgers vector and dislocation line for mixed and edge dislocations. As a consequence, compressive strain components may be parallel to the transversal magnetic field.

4 Conclusions

A significant increase of the drain current is proved if defined numbers and types of pure dislocations are placed in the channel of MOSFETs and directly connected to source and drain. An increase of the drain current of pMOSFETs by a factor of eight was found if mixed dislocations are present. The drain current enhancement is caused by a higher concentration and higher mobility of holes through dislocations. It is shown that mixed dislocations possess uniaxial compressive strain components in the order $\varepsilon \cong -0.1$ resulting in dramatic alterations of the band structure. The upper valence bands (heavy holes, light holes) are shifted upward and result in the formation of a quantum wire. **The formation of the quantum wire forces hole confinement along the dislocations and generates a one-dimensional hole gas.**

Acknowledgements We gratefully acknowledge S. Birner (nextnano GmbH, Poing) for helpful discussion.

References

- [1] D. Hull and D. J. Bacon, *Introduction to Dislocations* (Pergamon Press, Oxford, 1994).
- [2] D. B. Holt and B. G. Yacobi, *Extended Defects in Semiconductors* (Cambridge Univ. Press, Cambridge, 2007).
- [3] B. O. Kolbesen and H. Cerva, in: *Defects in Silicon III*, edited by T. Abe et al. (The Electrochemical Society, Pennington, NJ, 1999), Vol. PV 99-1, p. 19.
- [4] J. D. Murphy (ed.), *Gettering and Defect Engineering in Semiconductor Technology XV* (Trans Tech Publ., Zurich, 2014).
- [5] M. Reiche, M. Kittler, D. Buca, A. Hähnel, Q.-T. Zhao, S. Mantl, and U. Gösele, *Jpn. J. Appl. Phys.* **49**, 04DJ02 (2010).
- [6] M. Reiche, M. Kittler, H. Uebensee, E. Pippel, and S. Hopfe, *Adv. Nano Res.* **2**, 1 (2014).
- [7] M. Reiche, M. Kittler, W. Erfurth, E. Pippel, K. Sklarek, H. Blumtritt, A. Haehnel, and H. Uebensee, *J. Appl. Phys.* **115**, 194303 (2014).
- [8] W. T. Read, *Philos. Mag.* **45**, 775 (1954).
- [9] R. Labusch and W. Schröter, in: *Dislocations in Solids*, edited by F. R. N. Nabarro (North-Holland, Amsterdam, 1980), Vol. 5, p. 127.
- [10] H. Veth and M. Lannoo, *Philos. Mag. B* **50**, 93 (1984).
- [11] J. Bardeen and W. Shockley, *Phys. Rev.* **80**, 72 (1950).
- [12] R. W. Keyes, *Solid State Phys.* **11**, 149 (1960).
- [13] W. Schröter and H. Cerva, *Solid State Phenom.* **85-86**, 67 (2002).
- [14] H. Alexander and H. Teichler, in: *Materials Science and Technology*, edited by R. W. Cahn, P. Haasen and E. J. Kramer (VCH, Weinheim, 1991), Vol. 4, p. 249.
- [15] M. Reiche, M. Kittler, M. Krause, and H. Uebensee, *Phys. Status Solidi C* **10**, 40 (2013).
- [16] M. Reiche, M. Kittler, H. Uebensee, E. Pippel, A. Haehnel, and S. Birner, submitted to *Phys. Rev. B* (2014).
- [17] H. Alexander, H. Gottschalk, and C. Kisielowski-Kemmerich, in: *Dislocations in Solids*, edited by H. Suzuki et al. (University of Tokyo Press, Tokyo, 1985), p. 337.
- [18] A. T. Blumenau, PhD thesis, Univ. Paderborn, 2002.
- [19] C. W. Zhao and Y. M. Xing, *Proc. SPIE* **7375**, 737508 (2009).
- [20] S. Metz, Thesis, Univers. Frankfurt (Main), 2004.
- [21] S. Birner, T. Zibold, T. Andlauer, T. Kubis, M. Sabathil, A. Trellakis, and P. Vogl, *IEEE Trans. Electron. Devices* **54**, 2137 (2007).
- [22] J.-M. Jancu, R. Scholz, F. Beltram, and F. Bassani, *Phys. Rev. B* **57**, 6493 (1998).
- [23] M. V. Fischetti, Z. Ren, P. M. Solomon, M. Yang, and K. Rim, *J. Appl. Phys.* **94**, 1079 (2003).
- [24] D. Yu, Y. Zhang, and F. Liu, *Phys. Rev. B* **78**, 245204 (2008).
- [25] C. Lombardi, S. Manzini, A. Saporito, and M. Vanzi, *IEEE Trans. Comp. Aid. Design* **7**, 1154 (1992).
- [26] D. B. M. Klaassen, *Solid State Electron.* **35**, 953 (1992).
- [27] D. B. M. Klaassen, *Solid State Electron.* **35**, 961 (1992).
- [28] C. Koch, Thesis, Arizona State University, 2002.
- [29] A. H. Cottrell, *Phil. Mag. Ser. 7* **43**, 645 (1952).
- [30] M. Couillard, G. Radtke, and G. A. Botton, *Philos. Mag.* **93**, 1250 (2013).
- [31] V. Sverdlov, *Strain-induced Effects in Advanced MOSFETs* (Springer, Wien, 2011).
- [32] E. X. Wang, P. Matagne, L. Shifren, B. Obradovic, R. Kotlyar, S. Cea, and M. Stettler, *IEEE Trans. Electron. Devices* **53**, 1840 (2006).
- [33] K. Matsuda, in: *10th Int. Workshop on Computational Electronics* (IEEE, Piscataway, 2004), p. 173.
- [34] G. Sun, Y. Sun, T. Nishida, and S. E. Thompson, *J. Appl. Phys.* **102**, 084501 (2007).
- [35] M. S. Lundstrom, *Fundamentals of Carrier Transport* (Cambridge University Press, Cambridge, 2000).
- [36] W. Lu, J. Xiang, B. P. Timko, Y. Wu, and C. M. Lieber, *PNAS* **102**, 10046 (2005).